Earth and Planetary Science Letters 488 (2018) 168–180

Contents lists available at ScienceDirect

Earth and Planetary Science Letters

www.elsevier.com/locate/epsl

Imaging the Laguna del Maule Volcanic Field, central Chile using magnetotellurics: Evidence for crustal melt regions laterally-offset from surface vents and lava flows

Darcy Cordell [a,*], Martyn J. Unsworth [a], Daniel Díaz [b,c]

[a] Department of Physics, University of Alberta, Edmonton, T6E 2E1, Canada
[b] Departamento de Geofísica, Universidad de Chile, Blanco Encalada 2002, Santiago, Chile
[c] Centro de Excelencia en Geotermia de Los Andes, Plaza Ercilla 803, Santiago, Chile

ARTICLE INFO

Article history:
Received 26 September 2017
Received in revised form 5 January 2018
Accepted 9 January 2018
Available online 2 March 2018
Editor: P. Shearer

Keywords:
magnetotellurics
volcanism
southern volcanic zone
magma reservoir
hydrothermal reservoir

ABSTRACT

Magnetotelluric (MT) data were collected at the Laguna del Maule volcanic field (LdMVF), located in central Chile (36°S, 70.5°W), which has been experiencing unprecedented upward ground deformation since 2007. These data were used to create the first detailed three-dimensional electrical resistivity model of the LdMVF and surrounding area. The resulting model was spatially complex with several major conductive features imaged at different depths and locations around Laguna del Maule (LdM). A near-surface conductor (C1; 0.5 Ωm) approximately 100 m beneath the lake is interpreted as a conductive smectite clay cap related to a shallow hydrothermal reservoir. At 4 km depth, a strong conductor (C3; 0.3 Ωm) is located beneath the western edge of LdM. The proximity of C3 to the recent Pleistocene-to-Holocene vents in the northwest LdMVF and nearby hot springs suggests that C3 is a hydrous (>5 wt% H_2O), rhyolitic partial melt with melt fraction >35% and a free-water hydrothermal component. C3 dips towards, and is connected to, a deeper conductor (C4; 1 Ωm). C4 is located to the north of LdM at >8 km depth below surface and is interpreted as a long-lived, rhyolitic-to-andesitic magma reservoir with melt fractions less than 35%. It is hypothesized that the deeper magma reservoir (C4) is providing melt and hydrothermal fluids to the shallower magma reservoir (C3). A large conductor directly beneath the LdMVF is not imaged with MT suggesting that any mush volume beneath LdM must be anhydrous (<2 wt% H_2O), low temperature and low melt fraction (<25%) in order to go undetected. The presence of large conductors to the north has important implications for magma dynamics as it suggests that material may have a significant lateral component (>10 km) as it moves from the deep magma reservoir (C4) to create small, ephemeral volumes of eruptible melt (C3). It is hypothesized that there may be a north–south contrast in physical processes affecting the growth of melt-rich zones since major conductors are imaged in the northern LdMVF while no major conductors are detected beneath the southern vents. The analysis and interpretation of features directly beneath the lake is complicated by the surface conductor C1 which attenuates low-frequency signals. The attenuation from C1 does not affect C3 or C4. At 1 km depth directly beneath LdM, a weak conductor (C2; <10 Ωm) is imaged but is not required by the data. Forward modeling tests show that a relatively large (30 km^3), high melt fraction (>50%), silicic reservoir with 5 wt% H_2O at 2 to 5 km depth beneath the inflation center is not supported by the MT data. However, a smaller (10 km^3) eruptible volume could go undetected even with relatively high melt fraction (>50%). The location of large melt regions to the north has important implications for long-term volcanic hazards at LdMVF as well as other volcanoes as it raises the possibility that the vent distribution is not always indicative of the location of deeper source regions of melt.

© 2018 Elsevier B.V. All rights reserved.

1. Introduction

Large silicic magma systems have been the subject of intensive study due to their potential to cause very large, explosive eruptions (Self, 2006). However, it is still uncertain what causes these systems to develop and persist in the upper crust and what may

* Corresponding author.
E-mail addresses: dcordell@ualberta.ca (D. Cordell), unsworth@ualberta.ca (M.J. Unsworth), ddiaz@dgf.uchile.cl (D. Díaz).

https://doi.org/10.1016/j.epsl.2018.01.007
0012-821X/© 2018 Elsevier B.V. All rights reserved.

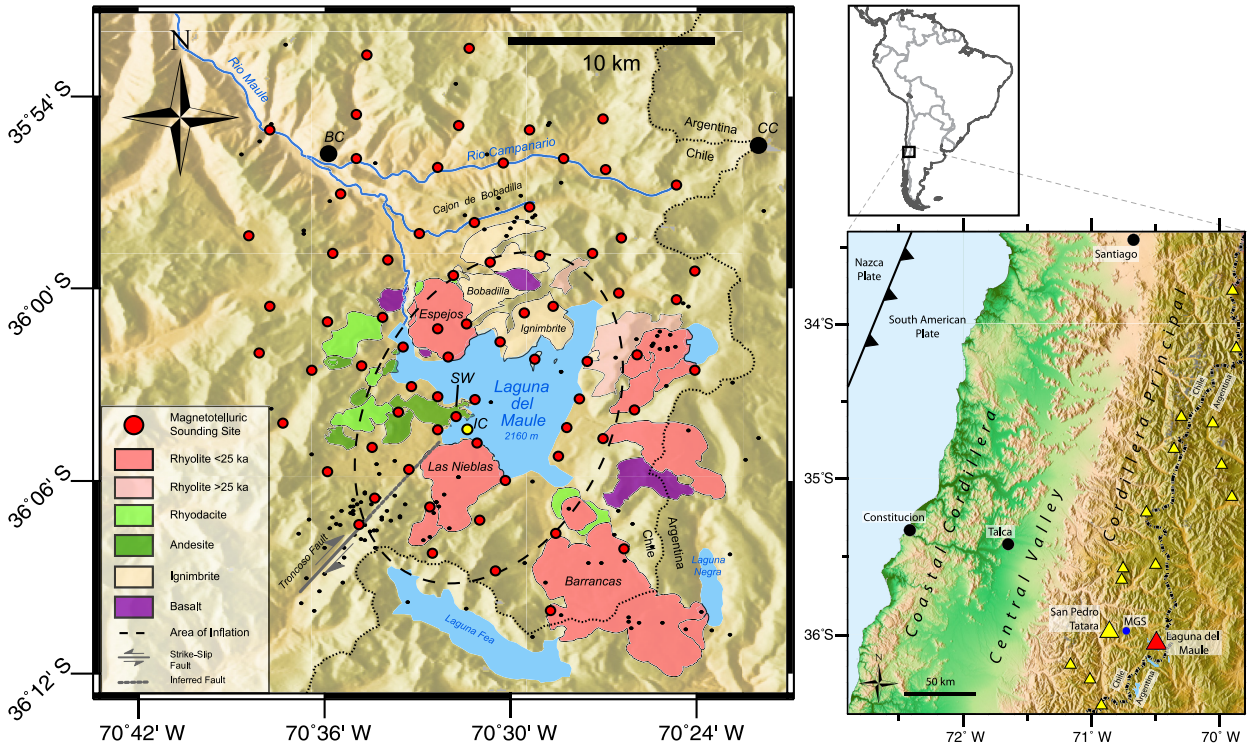

Fig. 1. Map of the study area around the Laguna del Maule Volcanic Field. Red dots are magnetotelluric sounding locations. The thick dashed line indicates the approximate area of observed inflation and the yellow dot (IC) denotes the point of maximum inflation as observed by InSAR (Feigl et al., 2013). Major lava flows are shown as colored polygons; the most recent (<25 ka) rhyolite flows are shown in dark pink (Andersen et al., 2017). Lava flows which are mentioned in the text are labeled on the map as is the southwest peninsula (SW) which is an important landmark. The inferred portion of the Troncoso Fault is shown as a dashed gray line. Small black dots are the locations of earthquakes with magnitude greater than 1 from 2011 to 2017 (Cardona et al., 2018). The thin dashed black line is the Chile–Argentina border. BC = Baños Campanario hydrothermal springs; CC = Cerro Campanario. The smaller regional map shows the location of Laguna del Maule as a red triangle along with San Pedro-Tatara Volcano (large yellow triangle) and Mariposa Geothermal System (MGS; blue circle) to the west. Small yellow triangles indicate other volcanos of the Southern Volcanic Zone. (For interpretation of the references to color in this figure, the reader is referred to the web version of this article.)

cause them to become unstable and erupt (Pritchard and Gregg, 2016). A better understanding of these systems is needed to determine the volcanic hazards they present.

The Laguna del Maule volcanic field (LdMVF; 36°S, 70.5°W) is located on the Andean range crest of the Southern Volcanic Zone in central Chile (Fig. 1). It includes a high concentration of basaltic-to-rhyolitic lava surrounding Laguna del Maule (LdM), an alpine lake at 2165 m above sea level (a.s.l.) near the Chile–Argentina border. A 200 km^2 area of LdMVF has been experiencing rapid upward ground deformation since at least 2007 as indicated by InSAR and ground-based GPS observations (Feigl et al., 2013). Uplift rates have exceeded 25 cm/yr resulting in a net vertical displacement of nearly 2 m (Le Mével et al., 2016). InSAR deformation modeling suggests an inflation source located at a depth of approximately 5 km below lake surface which has been interpreted as the addition of material into the upper crust (Le Mével et al., 2016). Bouguer gravity data also show a large gravity low beneath the lake which has been modeled as a low density body at 2 to 5 km depth (Miller et al., 2017a). Seismicity has been detected around LdM with prominent swarms to the southwest near the Troncoso fault at an average depth of approximately 2 km below sea level (Fig. 1; Cardona et al., 2018).

The distribution of lava flows, previous caldera eruptions, ground deformation, and gravity anomalies suggests that the LdMVF sits above a restless magmatic system which has the potential for large, explosive eruptions. This magmatic system is hypothesized to be a large, laterally-extensive crystal-rich mush zone with the observed inflation caused by mass addition from a deeper crystal-poor basaltic source (Singer et al., 2014; Andersen et al., 2017).

To better understand this system, it is necessary to use geophysical methods to image the subsurface. Various geophysical methods indirectly measure different Earth properties such as density, acoustic velocity or electrical resistivity. Each method is important in giving a different view of the volcanic system depending on the Earth property the method is sensitive to. The electrical resistivity of the Earth is dependent on the presence and chemical composition of hydrothermal fluids and partial melt as well as other factors such as clay minerals, temperature, and pressure (Unsworth and Rondenay, 2013). As such, imaging the electrical resistivity of the subsurface beneath the LdMVF can give insight into the location, size and composition of fluids within this dynamic system.

Magnetotellurics (MT) is a passive electromagnetic geophysical method which is used to image the electrical resistivity of the subsurface by measuring the natural time-varying fluctuations of the Earth's electric and magnetic fields and inverting these data in the frequency domain (Chave and Jones, 2012). MT has been previously applied at other volcanos to identify magma bodies in the shallow crust, investigate deformation sources, and study shallow hydrothermal systems (e.g. Heise et al., 2010; Aizawa et al., 2014; Muñoz, 2014; Comeau et al., 2016). MT is suited to studying the LdMVF because it is able to locate zones of hydrothermal fluid and/or partial melt and place limits on the size and composition of inferred magma bodies.

2. Geological setting

The LdMVF is located approximately 25 km east of the active volcanic arc in a rear-arc extensional setting (Fig. 1; Hildreth et al.,

2010; Ramos et al., 2014). Volcanism is driven by the subduction of the Nazca Plate beneath the South American Plate (Ramos et al., 2014). To the west, San Pedro-Tatara Volcano and the associated Mariposa Geothermal System (MGS) are located on the modern volcanic arc (Fig. 1; Hickson et al., 2011). Hot springs are located to the northwest of the LdMVF at Baños Campanario and Termas del Medano which have chemical signatures suggesting a mixing between fluids from local magmatic reservoirs and meteoric water circulation (Benavente et al., 2016).

At least 130 vents have been identified in the LdMVF which have erupted more than 350 km^3 of material in the last 1.5 Ma (Singer et al., 2014). Basaltic-to-rhyolitic lava flows are widely distributed around LdM and a large ignimbrite deposit to the north provides evidence of a caldera-forming eruption 950 ka (Hildreth et al., 2010). The eruptions at LdMVF have occurred in two distinct phases: 1) prior to 25 ka, lavas were compositionally variable with a full suite of basaltic-to-rhyolitic products and 2) after 25 ka, lavas have been almost exclusively rhyolitic suggesting a change may have occurred in the magmatic processes upon de-glaciation of the Andes (Singer et al., 2014). Lava flows encircle the lake with the most recent eruption occurring 2 ka at a vent approximately 5 km south of the current inflation center and creating the Las Nieblas lava flow (Andersen et al., 2017).

Earlier petrological studies suggested that the eruptions derived from a single, large magma system (Hildreth et al., 2010). However, recent work by Andersen et al. (2017) presents a more complicated model with temporal and compositional variations between northwest and southeast lavas. They conclude that it is likely that the lavas are derived from a large, crystal-rich reservoir beneath the lake which has been periodically spatially-segregated into ephemeral, crystal-poor, eruptible magma volumes in the northwest and southeast.

3. Methodology

Magnetotelluric data are collected by making time-domain measurements of Earth's natural electric and magnetic fields. In the frequency domain, these fields can be related with Maxwell's equations using a rank 2 tensor of complex impedance

$$\begin{bmatrix} E_x(\omega) \\ E_y(\omega) \end{bmatrix} = \begin{bmatrix} Z_{xx}(\omega) & Z_{xy}(\omega) \\ Z_{yx}(\omega) & Z_{yy}(\omega) \end{bmatrix} \begin{bmatrix} H_x(\omega) \\ H_y(\omega) \end{bmatrix}$$

where ω is the angular frequency, Z is the complex impedance, E is the electric field strength, and H is the magnetic field strength (Chave and Jones, 2012). The complex impedance contains frequency-dependent information about the Earth where lower frequencies sample greater depths. The complex impedance is often presented as apparent resistivity (ρ_a) and phase (ϕ):

$$\rho_{a_{ij}} = \frac{1}{\omega\mu_0}|Z_{ij}|^2 \quad \text{and} \quad \phi_{ij} = \tan^{-1}(Z_{ij}).$$

During the austral summers of 2015 and 2016, 54 broadband MT stations were collected within the LdMVF and surrounding area. These data were collected using Metronix ADU-07 data loggers and MFS-07 induction coil magnetometers along with EFP-06 Pb–PbCl electrodes. Vertical magnetic transfer functions (i.e. tipper) data were also collected at some sites, but tipper data were not included in the present analysis or interpretation. Average grid station spacing was approximately 2 km, taking into account the difficulty of the terrain. Time series data were recorded for between 12 and 24 h. All sites were processed using the robust method with smoothing constraints of Larsen et al. (1996) and remote reference methods were applied when possible (Chave and Jones, 2012). Resulting impedance data covered a broad range of frequencies from 2600 Hz to 0.0005 Hz. In addition to this survey, 17 MT sites were included from a previous broadband MT array collected by Alterra Power Corporation in 2009 and 2010 using Phoenix MTU-5A instruments (Hickson et al., 2011). This resulted in a total of 71 MT sites with locations shown in Fig. 1 (Stations.kml here) and all data curves are shown in Supplementary Material 1. The overall data quality is good with low root-mean-square (r.m.s.) misfit using a 6% error floor when solving the idealized, analytical D+ solution for off-diagonal components (Parker and Whaler, 1981). The analytical D+ solution is a non-physical one-dimensional model which fits MT curves with minimum misfit and can be used to aid interpretation (Beamish and Travassos, 1992). Low D+ misfit values with small error floors are often, but not always, an indication of relatively smooth, low-noise impedance data (Parker, 2010). A summary of data quality parameters is given in Table 1. Pseudo-section frequency slices of the determinant of the impedance tensor are shown in Fig. 2 plotted as determinant average apparent resistivity and phase (Ranganayaki, 1984). The apparent resistivity is quite low (<10 Ωm) in both components at all frequencies in the area around the inflation center indicating relatively low resistivity at both shallow and deep depths. High phases at higher frequencies (10 Hz) around the inflation center indicate decreasing resistivity at shallow depth but lower phases at low frequencies indicate increasing resistivity at deeper depths. Low apparent resistivities and very high phases at low frequencies (<0.1 Hz) to the north of LdM suggest a strong conductor at depth to the north.

Table 1
Summary of bandwidth and D+ root mean square (r.m.s.) misfit for all 71 MT sites in the survey area.

Average bandwidth	1000 Hz to 0.002 Hz	
Maximum bandwidth	2600 Hz to 0.0005 Hz	
Overall D+ r.m.s. (6% Error)	Z_{xy} component 1.06	Z_{yx} component 1.02

The dimensionality of the data was investigated using phase tensor analysis from Caldwell et al. (2004). High beta-skew angles (>3°) at low frequencies (<0.1 Hz) suggest complex, three-dimensional (3-D) geoelectric structure at depth and necessitate a 3-D modeling approach (Fig. 2; Booker, 2014). At very low frequencies (0.01 Hz), phase tensors indicate a weakly-developed strike of N13°W as shown in rose diagrams in Fig. 2. This is in contrast to the N5°E regional geoelectric strike described by the 2-D MT study of Reyes-Wagner et al. (2017) at this latitude, which included data collection in the Central Valley and Cordillera Principal. This may be an indication of a change in structural setting between the Cordillera Principal and the extensional trough in which the LdMVF is located (Ramos et al., 2014). At higher frequencies, there is no clear geoelectric strike direction in the data.

The ModEM 3-D inversion package was used for all inverse modeling using finite difference methods and a non-linear conjugate gradient inversion algorithm (Kelbert et al., 2014). Both diagonal and off-diagonal impedance components were inverted. Various parameters were investigated and the primary resistivity features of the model were largely independent of chosen parameters (see Supplementary Material 2). The mesh shown has 500 m horizontal cells in the central region (35 km × 25 km) with 12 padding cells in each direction increasing gradually to cover a 425 km × 425 km model space. Since the LdMVF is located more than 200 km from the ocean, and the lowest frequency used was 0.0005 Hz, the ocean was not included in the model (see Reyes-Wagner et al. (2017) for a discussion of the ocean effect on regional data). Topography was included using 50 m cells and included 2700 m of topographic relief in the central region with a maximum elevation of 3875 m a.s.l. and minimum elevation of 1175 m a.s.l. The vertical cells increased gradually to a maximum

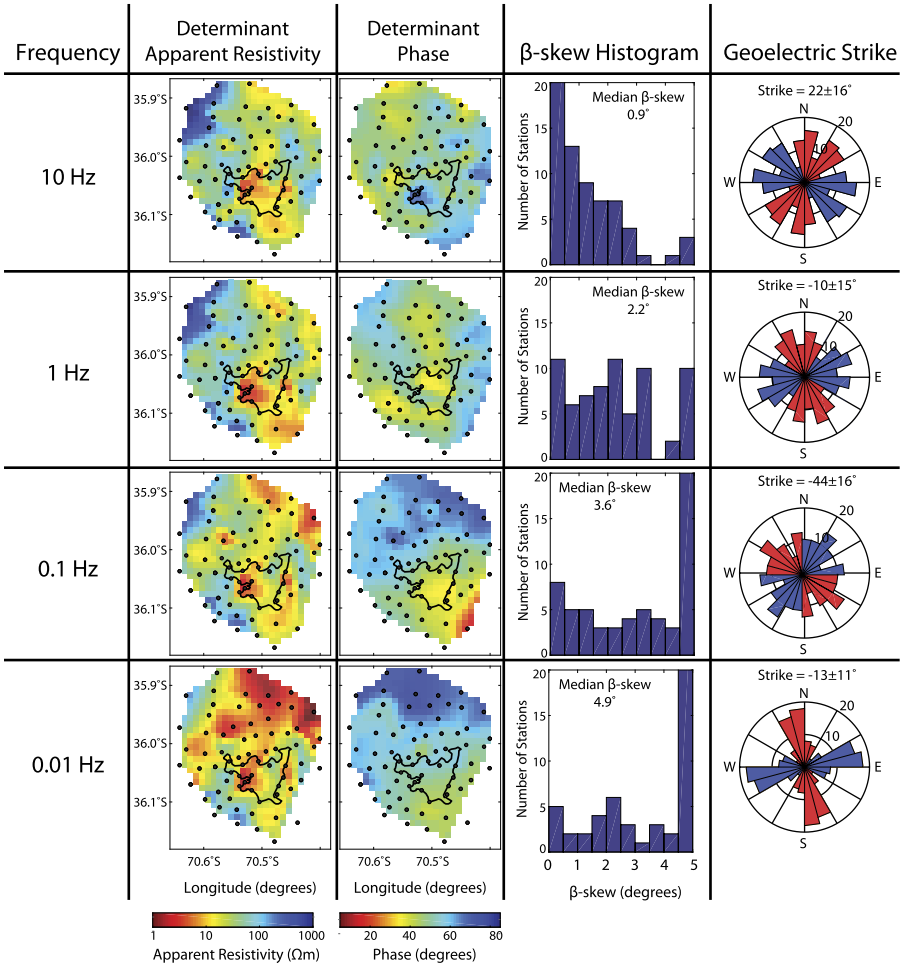

Fig. 2. Each row shows data at a different frequency (10 Hz, 1 Hz, 0.1 Hz, and 0.01 Hz) for the 71 MT sites. The first two columns show the interpolated apparent resistivity (column 1) and phase (column 2) data for the determinant average of the complex impedance with red indicating areas of low apparent resistivity and low phase, respectively. Black dots indicate MT site locations. The outline of Laguna del Maule is given as reference point. The third column shows histograms of β-skew angle which is a rotationally-invariant quantity calculated using the phase tensor (Caldwell et al., 2004). High β-skew angles ($>3°$) indicate 3-D geoelectric structures while skew angles $<3°$ suggest 1-D, 2-D or quasi-2-D structures (Booker, 2014). The final column shows rose histograms of strike angle calculated from phase tensor ellipse axes. Weakly developed geoelectric strike and relatively high skew values suggest largely 3-D structures over the survey area. (For interpretation of the references to color in this figure, the reader is referred to the web version of this article.)

depth of 700 km. The entire model volume was $98 \times 74 \times 124$ cells and the inversion was begun with an initial 100 Ωm halfspace starting model.

4. Results from the three-dimensional inversion of the MT data

The 3-D resistivity model obtained from inversion of the MT data is shown in Figs. 3 and 4. A satisfactory total r.m.s. misfit value of 1.46 was reached after 89 iterations using a 6% error floor on all impedance components. Error floors were chosen so that a D+ solution achieved a good fit without over-fitting or under-fitting the data (Table 1). This choice of error floor provides a benchmark when assessing the 3-D inversion response because an r.m.s. misfit of 1.0 corresponds to the best-fit of the D+ solution for all sites. The r.m.s. misfit is shown as a function of frequency and for each station in map view in Fig. 3(e) and 3(f), respectively. All data curves with model fit are shown in Supplementary Material 1. Higher r.m.s. misfit is generally found at stations on the edge of the array and at lower frequencies.

The resistivity model contains four primary conductive anomalies with resistivities less than 10 Ωm. Depths to anomalies are cited as depth below lake surface of LdM (2165 m a.s.l.). Because of the diffuse nature of the MT signal, the depth to a given feature is best determined by the inflection point of a depth-resistivity curve rather than the point of minimum resistivity as shown in synthetic studies (Comeau et al., 2016). Other weaker conductive features (>10 Ωm) are also present but these were often small, poorly constrained on the edge of the array, or weakly conductive and are not interpreted in the present work.

4.1. Surface LdM conductor (C1)

The entire surficial geoelectric structure is inhomogeneous and influenced by topography and local geology immediately adjacent to the MT site locations (Fig. 3(a)). The roughness of the surface layer may also be related to the inversion model generating structure to fit static shifts and related galvanic effects. The largest, most continuous feature is C1: a thin, near-surface, low-resistivity anomaly (<1 Ωm) at approximately 100 m depth (2.0 km a.s.l.). C1 is centered on the point of maximum observed inflation with additional zones of low resistivity to the southeast.

4.2. Shallow LdM conductor (C2)

C2 is a shallow, low-resistivity anomaly at approximately 1.0 km depth (1.1 km a.s.l.) which is also spatially coincident with the zone of maximum inflation (Fig. 3(b)). It has dimensions of 4 km by 3 km and a minimum resistivity of 1 Ωm. C2 does not appear

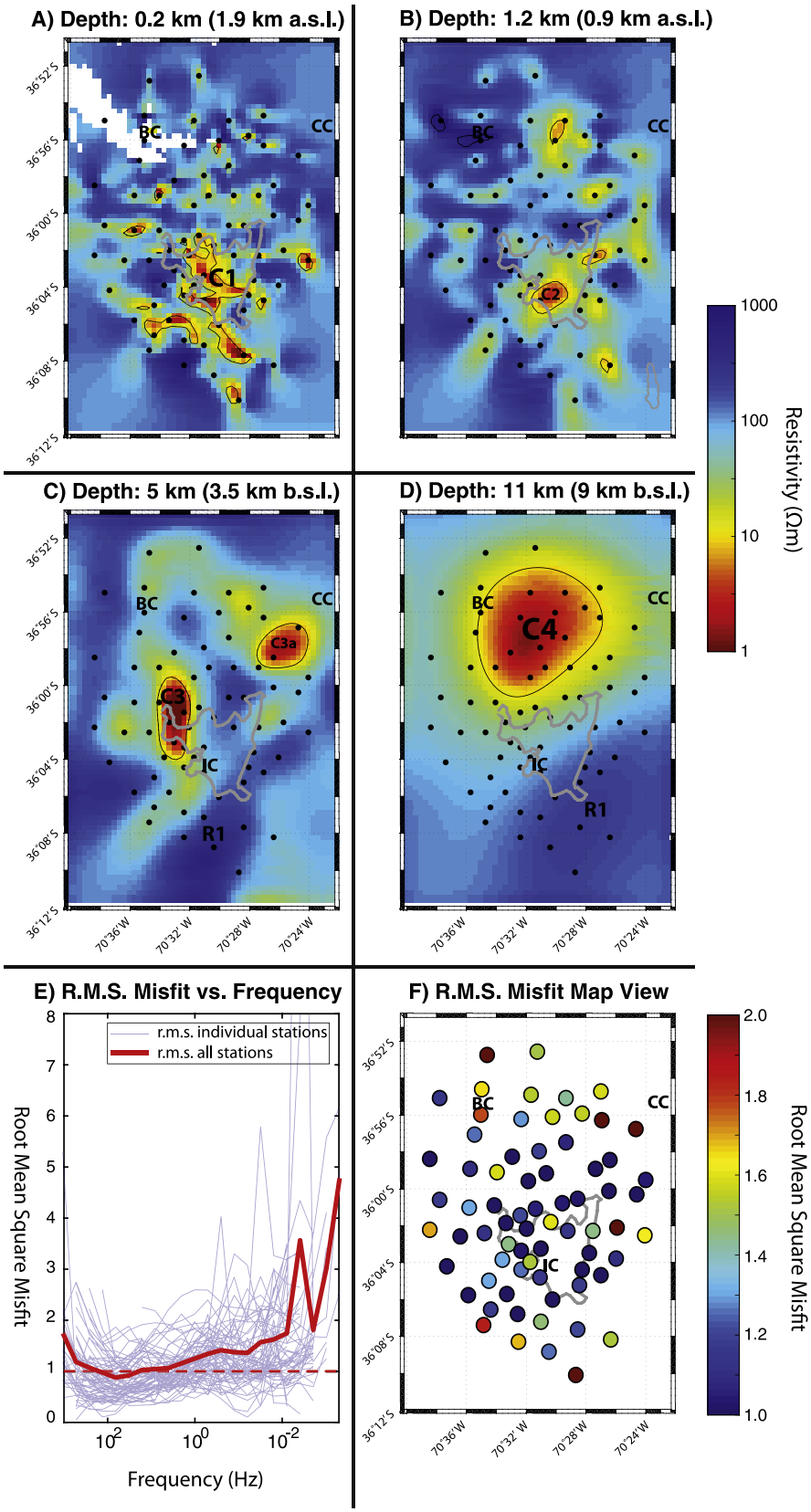

Fig. 3. Model results shown using 4 horizontal slices through the model at approximate depths of **(a)** 0.2 km below lake surface (b.l.s.; 1.9 km a.s.l.), **(b)** 1.2 km b.l.s. (0.9 km a.s.l.), **(c)** 5 km b.l.s. (3.5 km b.s.l.), and **(d)** 11 km b.l.s. (9 km b.s.l.). Major interpreted features are labeled C1, C2, C3, C3a, C4, and R1. On each slice: BC = Baños Campanario; IC = Inflation Center; CC = Cerro Campanario; and the outline of the lake is given for reference. White space is air (above topography surface). The thin lines on each slice represent the 10 Ωm contour. **(e)** Graph shows r.m.s. misfit as a function of frequency for all stations (light blue lines) and overall (thick red line). **(f)** Map shows station locations with circles colored as the r.m.s. misfit value at each station. Blue corresponds to low r.m.s. misfit and red corresponds to high r.m.s. misfit. (For interpretation of the references to color in this figure, the reader is referred to the web version of this article.)

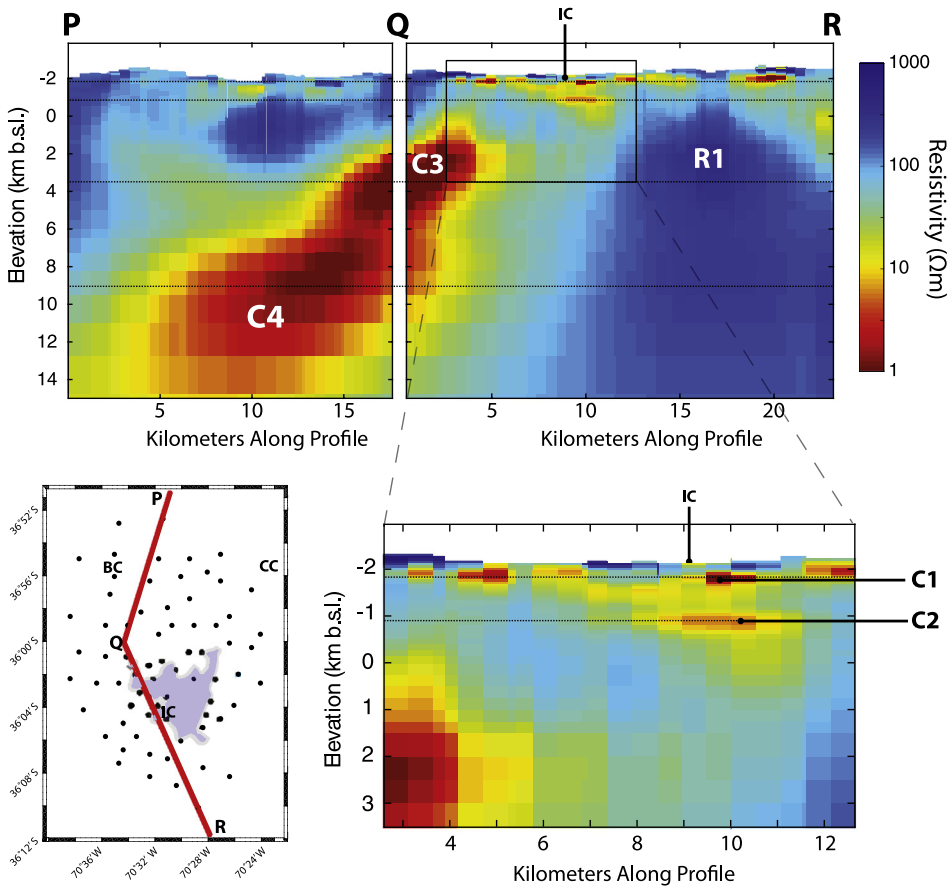

Fig. 4. Model results are shown using a fence diagram using two diagonal slices through the model along PQ and QR as shown in map inset. Black dots in the map inset denote MT sounding locations. Profile PQ cuts across major features C3 and C4. Profile QR cuts directly across the inflation center (IC) and shows the edge of C3, as well as C2 and C1. To show more detail of C1 and C2, a model inset is enlarged. The thin dashed lines through the profiles denote the depth locations of the horizontal slices shown in Fig. 3. BC = Baños Campanario; CC = Cerro Campanario; White space at top of profile is air cells above topography surface.

in all inversion tests and does not appear to be required in order to adequately fit the MT impedance data and thus may be an artifact.

4.3. Espejos conductor (C3) and Campanario conductor (C4)

To the north and northwest of the inflation center are two conductors (C3 and C4). C4 is the deepest low-resistivity feature in the model with a depth of 8–9 km (6–7 km b.s.l.) located beneath the Río Campanario Valley and Bobadilla Canyons (Fig. 3(d)). The minimum resistivity of C4 is approximately 1.5 Ωm. From C4, two conductive lobes extend towards the surface. The first lobe (Espejos Conductor; C3), extends upward at 45 degrees from the southwestern edge of C4, trending north–south beneath the Río Maule Valley (Fig. 3(c)). It terminates at a depth of approximately 3 km (1 km b.s.l.) beneath the western edge of the lake. This feature has a strong conductive signature (<0.3 Ωm) and was previously identified using preliminary MT data (Singer et al., 2014). The second lobe (C3a) extends from the eastern edge of C4 and trends southeast, terminating at 3 km depth near the 160 ka Cerro Campanario stratovolcano (Hildreth et al., 1998). Unfortunately, C3a is on the edge of the array and is less conductive than C3, so it is difficult to interpret. The apparent connection between C4 and shallower features (C3 and C3a) may be partly due to diffusive smoothing of the inversion algorithm as resolution decreases with depth, but may be indicative of a geological connection. A regional two-dimensional MT study of the electrical structure of central Chile at this latitude identified conductors at approximately the same location and depth as both C3 and C4 (Reyes-Wagner et al., 2017).

5. Geological interpretation and discussion

5.1. Interpretation of features within the area of observed ground deformation

There are two main features (C1 and C2) directly beneath LdM and the observed surface uplift. Since C1 is relatively shallow and spatially coincident with the lake bed, it is important to confirm that C1 is not due to free ions in the lake water. The electrical resistivity of the lake water was measured at four surface locations in 2017 and the measurements had an average value of 53 ± 5 Ωm. This suggests the water is fresh and fed primarily by snow melt, since most natural lakes have a range of resistivities from 10–50 Ωm where higher resistivity indicates low total dissolved solids (USGS, 2017). Therefore, considering the resistivity of the water is quite high, the lake itself cannot be the source of the conductive anomaly (C1). It is likely that this conductor is the result of conductive hydrothermal fluids and/or clay-bearing sediments similar to that found at other volcano-hydrothermal systems (Muñoz, 2014 and references therein). The resistivity is quite low suggesting either: 1) a high-salinity hydrothermal fluid; or 2) an altered smectite clay with high cation exchange capacity (Muñoz, 2014). If LdM were underlain by a shallow high-salinity reservoir, it would be expected that the lake water would be more saline due to fluid pathways between lake and shallow reservoir. As such, clay must play some role in the resistivity of the hydrothermal system and MT may be imaging the clay cap of the system. Smectite clay is indicative of the temperature of the hydrothermal fluid, with the smectite-illite transition occurring around 150 °C. Illite is more

resistive than smectite, so the low bulk resistivity of C1 suggests a reservoir temperature <150 °C (Muñoz, 2014). Heat and fluid may be supplied from the deeper conductive features C3 and C4 (see Section 5.2). The presence of hydrothermal fluids at depths of 1.5 km has also been confirmed by time-lapse gravity studies (Miller et al., 2017b). While it is unlikely that MT would be able to detect a thin opening related to the time-lapse gravity, the MT data may be detecting a more long-lived, shallow hydrothermal zone beneath the lake.

The MT model shows a relatively weak conductor (C2) at 1 km depth directly below the center of inflation but the feature does not appear in all inversion models. In general, MT requires that the conductance (i.e. product of thickness and conductivity) of an underlying layer is greater than the overlying layer in order to be detected with confidence (Jones, 1999). The maximum conductance of C1 is approximately 400 S. The maximum conductance of C2 is also 400 S and is therefore on the limit of detection and, without further constraints, could be considered an artifact. Removing C2 has very little effect on data fit and is primarily constrained by only one station (LDM049). The anomalies C3 and C4 both have maximum conductance values >5000 S and neither underlie C1, so C1 has no effect on the imaging of these features.

5.1.1. Incorporating previous Bouguer gravity results

Miller et al. (2017a) show that a 30 km^3, 3 km-thick, crystallinity-zoned magma reservoir with 50–85% rhyolitic melt from 2–5 km depth located directly beneath the lake is consistent with the Bouguer gravity data. This additional constraint suggests that C2 may be a poorly-resolved portion of a larger anomaly or an additional hydrothermal system overlying the anomaly imaged by Miller et al. (2017a). However, it is surprising that MT does not image a large conductor in the same spatial location as the anomaly of Miller et al. (2017a) since both MT and gravity methods should be sensitive to melt. As such, a sensitivity analysis is necessary to assess whether such a magma body as described by Miller et al. (2017a) could go undetected with MT. By adding a conductive anomaly which matches the size, location, and composition of the magma body inferred from the Bouguer gravity data, forward modeling tests can be used to compare the computed MT response of the edited model to the original data and inversion model response.

To do this, the resistivity of the modeled density anomaly must be estimated based on the water content, silica content and temperature of the melt. Pressure also plays a role but, for the pressures under consideration (50–200 MPa), any effect of pressure is negligible (Unsworth and Rondenay, 2013). Since the magma reservoir is likely to be crystallinity-zoned, a simplified two-layer magma reservoir is assumed (Andersen et al., 2017; Miller et al., 2017a). The top layer is a 500 m-thick, 85% rhyolitic melt between 790 °C and 850 °C with 5 wt% H_2O. The lower layer is a 2.5 km-thick, 5 wt% H_2O, 50% dacitic melt between 790 °C and 850 °C. The temperature and water content ranges are taken from Miller et al. (2017a) to allow for direct comparison. The silica content and thickness of each layer is somewhat arbitrary based on the assumption that fractionation is occurring with silica-rich, high-melt fraction components collecting near the top of the reservoir. Using the empirical relation for rhyolite from Guo et al. (2016), the average pure melt resistivity of Layer 1 is estimated to be approximately 0.4 Ωm (Fig. 5(a)). The empirical relationship for dacitic melt from Laumonier et al. (2015) is used for Layer 2 resulting in an average pure melt resistivity of approximately 2.2 Ωm (Fig. 5(b)). The final step is to calculate the bulk resistivity of the partial melt using Modified Archie's Law (MAL) from Glover et al. (2000):

$$\sigma_b = \sigma_f \phi^m + \sigma_h (1-\phi)^p$$

where

$$p = \frac{\log(1-\phi^m)}{\log(1-\phi)}$$

and σ_b is the bulk conductivity, σ_f is the fluid conductivity, σ_h is the host rock conductivity, ϕ is the melt fraction, and m is the connectivity parameter. For most rocks, the value of m lies between $m = 1.5$ (well-connected) to $m = 2.5$ (poorly-connected). For the melt fractions under consideration, it can be assumed that the melt is well-connected and a value of $m = 1.5$ is used (Rosenberg and Handy, 2005). Using MAL, the estimated bulk resistivity of Layer 1 is approximately 0.5 Ωm while for Layer 2 the average value is 6 Ωm (Fig. 6).

To test whether such an anomaly could be detected, a layered resistivity anomaly (G1) was added to the MT inversion model with the same dimensions and location as the −600 kg/m^3 Bouguer density isosurface from Miller et al. (2017a) (Fig. 7). The exact volume of G1 is 28 km^3 after interpolation. The maximum conductance of the anomaly was 1400 S. The depth to the anomaly is less than the width and the conductance is quite large so on initial inspection it seems that the anomaly should have an MT response based on previous studies of magma bodies (Newman et al., 1985). The MT impedance response was computed for the edited model and compared to the inversion response of the original model and MT data.

Fig. 7 shows the results of this forward modeling experiment and highlights site LDM013, located on the southwestern peninsula, which showed the greatest increase in r.m.s. misfit between the inversion response and the computed response of the edited model. At this site, the r.m.s. misfit ratio (i.e. the ratio between the misfit from the edited model divided by the misfit from the original model) was 2.29 indicating the misfit more than doubled (from 0.82 in the original model to 1.88 in the edited model). This suggests a much poorer fit when the gravity anomaly is added. As can be seen in Fig. 7, the high frequencies are still fit well for the off-diagonal impedance components but at frequencies less than 1 Hz, the computed response no longer fits the measured data. The diagonal components are generally much noisier than the off-diagonal components at all sites (see Supplementary Material 1) and this is true of LDM013 as well. The inversion fails to fit the diagonal components at high frequencies (>10 Hz) whether G1 is added or not. Importantly, when G1 is added, the fit to the diagonal components also becomes worse at lower frequencies (<0.1 Hz). In Fig. 7, the r.m.s. misfit ratio for each station is shown in map view. This highlights the spatial sensitivity of the added gravity anomaly. This modeling test shows large increases in r.m.s. misfit when the G1 anomaly is added suggesting that a 30 km^3, 50 to 85% melt fraction anomaly is not consistent with the MT data.

Since Bouguer gravity shows a clear data anomaly, it is useful to ask how small or how resistive an anomaly would need to be to go undetected by the MT data. To test this, three different sized anomalies at 2 km depth were investigated with different bulk resistivity values. A 30 km^3 anomaly (G30) was set to have bulk resistivity values of 0.3, 0.5, 1, 3, 10, and 30 Ωm. These bulk resistivities correspond to rhyolite melt fractions of roughly 100%, 85%, 50%, 25%, 10%, and 5%, respectively assuming a 0.4 Ωm melt resistivity (see Fig. 6). The same bulk resistivity values were applied to two smaller features: a 20 km^3 anomaly (G20), and a 10 km^3 anomaly (G10) (see Supplementary Material 3). Fig. 8 shows the r.m.s. misfit ratio for each MT station as a function of bulk resistivity for the anomaly. As can be seen in Fig. 8, most stations have an r.m.s. misfit ratio near 1 regardless of the composition or size of the anomaly. This is due to the fact that most stations are far from the anomaly and cannot detect it. However, there is a general upward trend in the r.m.s. misfit ratio as the bulk resistivity

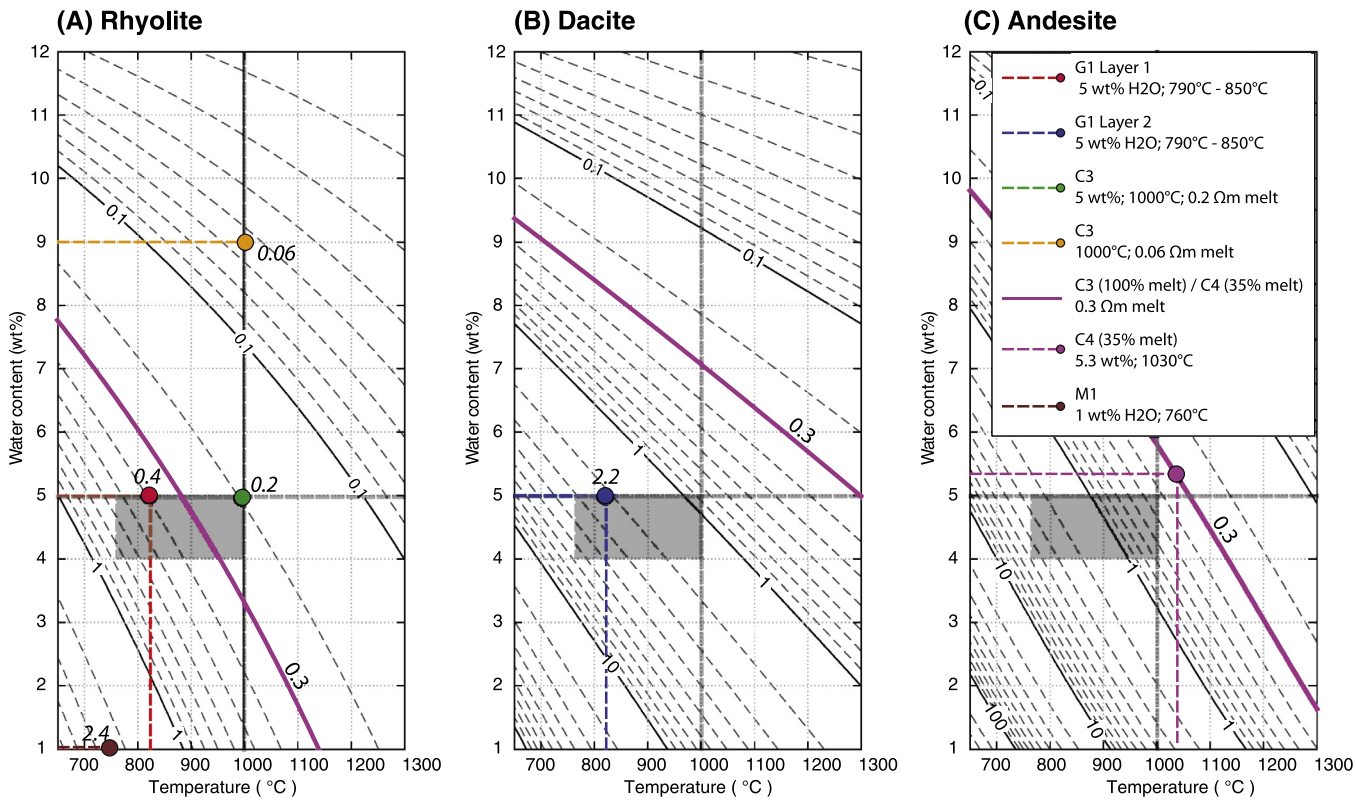

Fig. 5. Water content as a function of temperature with contours of melt resistivity used for interpretation of features in text. On all plots, the gray box denotes the temperature and water content ranges based on petrological estimates from Andersen et al. (2017). **(a)** Water content vs. temperature relationship with contours of melt resistivity for rhyolite melt (Guo et al., 2016). This graph is used to estimate the melt resistivity of G1 (Layer 1; 0.4 Ωm) and M1 (2.4 Ωm) given temperature and water content constraints. It is also used to estimate the minimum melt resistivity of C3 (0.2 Ωm) given petrological constraints and to show that water content would need to be high (9 wt%) to achieve a melt resistivity of 0.06 Ωm. For C4, the maximum melt resistivity contour (0.3 Ωm) is shown which corresponds to <35% melt fraction (from Fig. 6). **(b)** Water content vs. temperature relationship with contours of melt resistivity for dacite melt (Laumonier et al., 2015). This graph is used to estimate the resistivity of G1 (Layer 2; 2.2 Ωm) given temperature and water constraints. It is also used to show that C3 is difficult to explain as a dacite melt because the 0.3 Ωm melt resistivity contour represents 100% melt and does not pass through the gray box. Similarly, a 0.3 Ωm melt resistivity corresponds to a 35% melt fraction for C4 (see Fig. 6) and so it is difficult to explain C4 as a dacite unless the melt resistivity (and melt fraction) are higher. **(c)** Water content vs. temperature relationship with contours of melt resistivity for andesite melt (Guo et al., 2017). This graph is used to show that it is difficult to explain C3 as andesite given petrological constraints because the 0.3 Ωm melt resistivity contour (corresponding to 100% melt fraction) does not pass through the gray box. It is possible to explain C4 as a low melt-fraction (<35%) andesite if temperatures or water contents are slightly beyond petrological estimates (e.g. 1030 °C and 5.3 wt% water). A constant pressure of 100 MPa was used for all estimates.

of a given anomaly is decreased and as the size is increased. Fig. 8 highlights LDM013, which had the greatest increases in r.m.s. misfit. In order to keep the r.m.s. misfit ratio at LDM013 relatively low (e.g. <2), G30 needs to have a bulk resistivity greater than approximately 5 Ωm. This corresponds to a rhyolitic magma body with a melt fraction less than 25%. In contrast, a small, 10 km^3 anomaly (G10) is outside the resolution limits of the current MT array and sees almost no change in r.m.s. misfit, even at relatively high melt fraction (e.g. >50% melt). The maximum conductance of G10 is greater than the conductance of C1 for resistivity values of 0.3, 0.5, and 1 Ωm. A 20 km^3 anomaly could also go undetected but would need lower melt fraction (e.g. <50% melt). This exercise provides a range of possible models which are consistent with the MT results while excluding certain models as inconsistent. More complete data curves are shown in Supplementary Material 3.

A final possibility to consider is that the temperature of the melt has a very strong effect on both the density and resistivity of the magma body. Recent petrological estimates from Andersen et al. (2017) suggest melt temperatures could be as low as 760 °C. If the magma temperature is low, it could result in increased bulk resistivity and decreased bulk density which would make gravity data more sensitive to the anomaly while making electrical data less sensitive to the anomaly. The lack of a strong electrical signature in the MT data provides an important constraint on the available geological interpretations of the LdMVF magma system.

5.1.2. Deep inflation source

The MT inversion does not image any conductor with the same location or depth as the inflation source modeled by Feigl et al. (2013) or Le Mével et al. (2016). The inflation source is modeled as either a 9 km by 5 km basaltic sill oriented north–northeast at 5 km depth or a penny-shaped crack with radius of 6.2 km and depth of 4.5 km. Over the course of 7 yrs of observation, an estimated 0.19 km^3 of material has been injected (Le Mével et al., 2016). Simple geometric estimates suggest an opening of between 1 to 4 m. Using the empirical relation of Ni et al. (2011), a resistivity of 0.1 Ωm for a pure basaltic melt injection is a reasonable approximation. However, even with a highly-conductive, pure melt injection, a 4 m thick sill could not be imaged by the MT data. Taking into account the potential attenuation by C1, the limiting thickness for resolving such a feature at 5 km depth is >20 m given a simplistic, ideal 1-D assumption (Supplementary Material 4).

5.2. Interpretation of features outside the area of observed inflation

5.2.1. North of LdM

The Espejos Conductor (C3) is the most robust feature in the MT model and was detected in prior, less detailed 2-D and 3-D MT studies (Singer et al., 2014; Reyes-Wagner et al., 2017). Given the proximity to both the recent basaltic-to-rhyolitic vents in the northwest, the 950 ka Bobadilla caldera, and the saline Baños

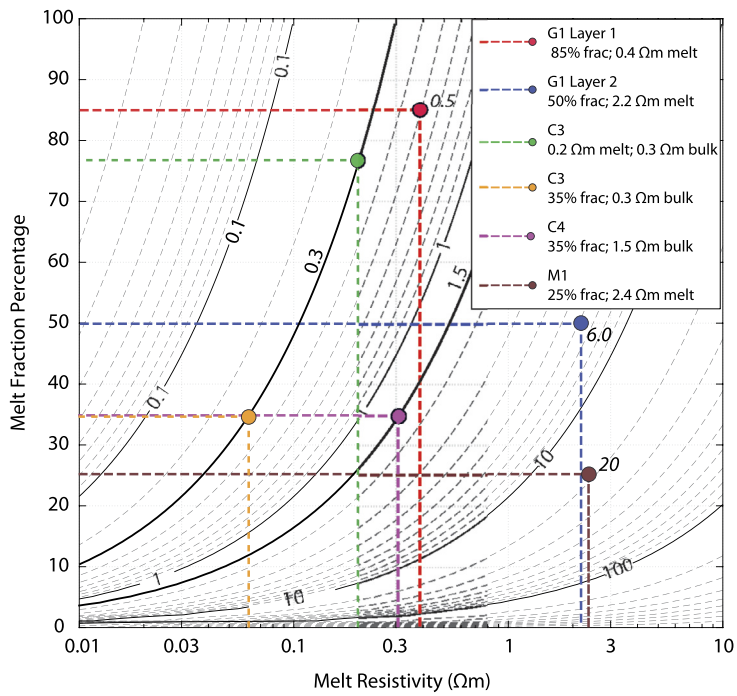

Fig. 6. Modified Archie's Law (MAL; Glover et al., 2000) plotted as melt fraction vs. melt resistivity with contours of bulk resistivity for $m = 1.5$. This graph is used to estimate the bulk resistivity of G1 Layer 1 (0.5 Ωm), G1 Layer 2 (6 Ωm), and M1 (20 Ωm) based on the melt resistivities estimated from Fig. 5(a) and 5(b). It is also used to estimate the minimum melt fraction (75%) for C3 based on petrological estimates of rhyolite melt resistivity from Fig. 5(a). Finally, it is used to estimate the melt resistivity of C3 (0.06 Ωm) and C4 (0.3 Ωm) necessary to achieve melt fractions <35%.

Campanario hot springs, it is possible that C3 and/or C4 could be partial melt, hydrothermal fluids, hydrothermal alteration, or some combination. The depth of C4 at approximately 9 km below surface (7 km b.s.l.) supports a magmatic interpretation since this is a common depth at which partial melt accumulates at the upper-to-middle crust boundary (Chaussard and Amelung, 2014). The distribution of seismicity can also constrain the depth of the brittle-ductile transition (Ogawa et al., 2014). While there is significant seismicity to the southwest of LdM along the Troncoso fault at 3 to 5 km depth (Fig. 1), there is a notable lack of seismicity to the north of LdM (i.e. near C3 or C4) which may suggest a hotter, more ductile zone. C3 could be interpreted as a hydrothermal system of exsolved fluids related to C4 (Newman et al., 1985). However, given the inferred melt present in G1 (at shallower depth than C3; Miller et al., 2017a) and the lack of seismicity it seems likely that C3 contains some amount of partial melt.

There is no clear Bouguer gravity signature associated with C3 or C4 (Miller et al., 2017a). For C4, this can be explained by the lack of gravity stations north of the lake. The lack of gravity signature associated with C3 can be used as an additional constraint on the composition suggesting that C3 is a higher density anomaly nearer to the 2400 kg/m^3 background density used by Miller et al. (2017a).

The minimum bulk resistivity of C3 is low (0.3 Ωm) which is difficult to explain without including large amounts of dissolved water in the melt to increase the conductivity (Laumonier et al., 2017). Andersen et al. (2017) give petrological estimates for the temperature range of 760 °C to 1000 °C and water contents of 4–5 wt% for erupted lavas at the LdMVF. Using the empirical relation for rhyolite from Guo et al. (2016), it can be seen that the estimated melt resistivity would be between 0.2 Ωm and 0.8 Ωm (gray box in Fig. 5(a)). Given the modeled bulk resistivity of C3 (0.3 Ωm), these melt resistivity values correspond to melt fractions greater than 75% (Fig. 6). The empirical relations for dacite (Fig. 5(b); Laumonier et al., 2015) or andesite (Fig. 5(c); Guo et al., 2017) cannot explain the modeled bulk resistivity for C3 even with 100% melt, unless water content or temperature are significantly higher. A rhyolite melt fraction of 75% is quite high for such a large, shallow anomaly and in order to arrive at a lower melt fraction estimate, either temperature or water content (or both) must be higher. An increase in either parameter is not supported by petrological data but, by their nature, such data can only sample previously erupted material and may not be indicative of magma storage conditions today, especially if eruptible reservoirs are ephemeral. Furthermore, aqueous fluids in subduction zones have been widely studied and should not be ruled out as an explanation (e.g. Wannamaker et al., 2014; Laumonier et al., 2017). The presence of nearby hot springs with strong magmatic signature is further evidence that water is present in the upper crust (Benavente et al., 2016). It is possible that C3 is a magma-hydrothermal system composed of both hydrous partial melt and free-water hydrothermal fluids. For example, if the magma-hydrothermal system included 9 wt% water, then the melt fraction could be less than 35% (Fig. 5(a) and Fig. 6).

For C4, a similar analysis was undertaken where the minimum modeled bulk resistivity of 1.5 Ωm is greater than for C3. Thus C4 can be explained with a relatively low melt fraction without invoking high water contents. In terms of volcanic hazards, an important question to ask is whether C4 could be considered a large eruptible volume of relatively crystal-poor magma. In order to be considered an eruptible volume, the melt fraction should be greater than 35% at which point the viscosity of the reservoir becomes low enough to allow it to flow (Bachman and Bergantz, 2008). For this to be the case for C4, using MAL, the melt resistivity would need to be greater than 0.3 Ωm (Fig. 6). The 0.3 Ωm melt resistivity contour is highlighted in Fig. 5 for the empirical relations for rhyolite (Guo et al., 2016), dacite (Laumonier et al., 2015) and andesite (Guo et al., 2017). As can be seen in Fig. 5(a), this melt resistivity contour passes through the range of petrological estimates from Andersen et al. (2017) and suggests that C4 could be explained as a relatively low melt fraction crystal-rich rhyolite mush which is not currently eruptible. However, both dacite and andesite melts would require

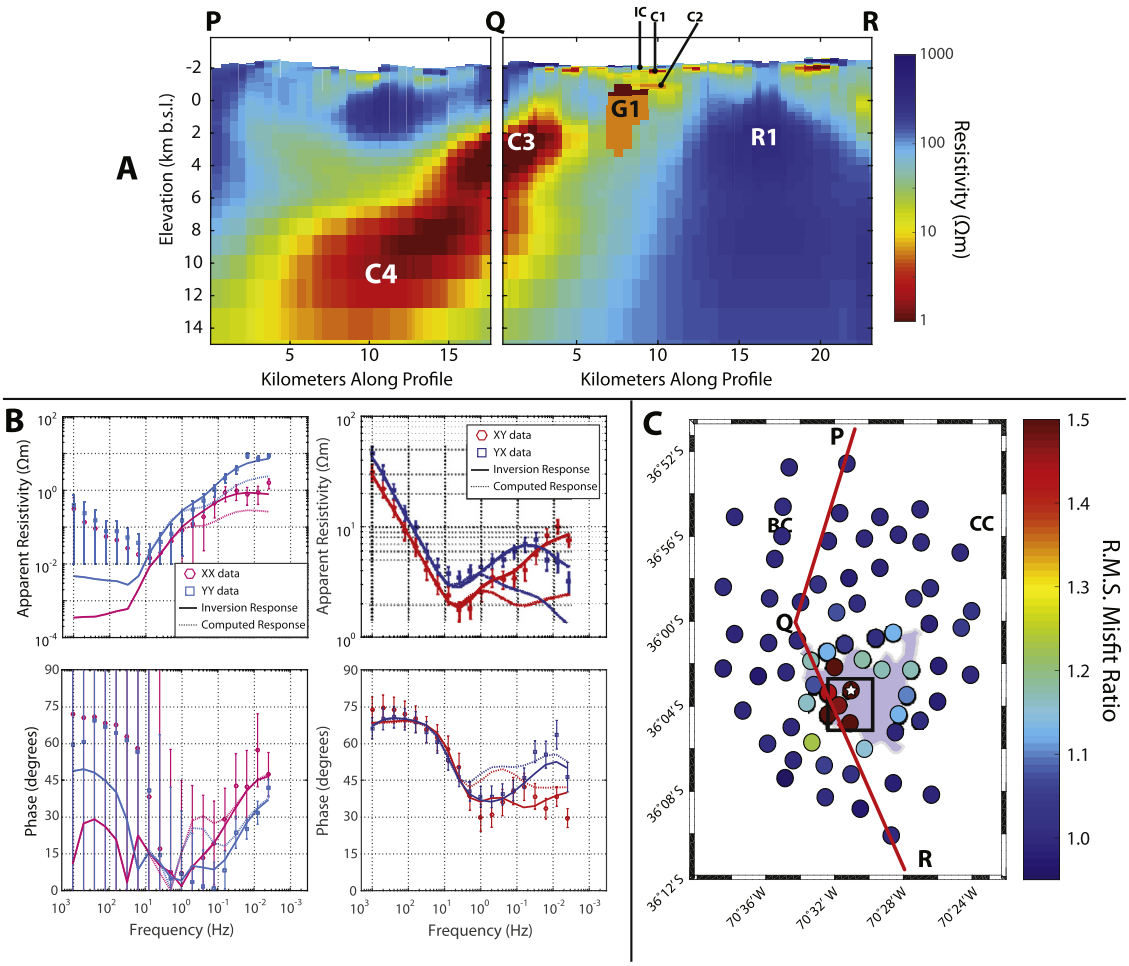

Fig. 7. Sensitivity analysis for a layered, 30 km^3 resistivity anomaly (G1) with a maximum conductance of 1400 S. The anomaly has the same dimensions and location as the preferred gravity model described in Miller et al. (2017a). Layer 1 has resistivity of 0.5 Ωm, Layer 2 has resistivity of 6.0 Ωm. See text for more details. **(a)** The top panel shows the same diagonal fence diagram from Fig. 4 along PQR through the inversion model with the G1 anomaly added. **(b)** The apparent resistivity and phase of the impedance tensor components as a function of frequency for site LDM013. The red and pink hexagons with errors bars show the xy and xx data, respectively, as a function of frequency. The blue and light blue circles with error bars show the yx and yy data, respectively. The solid lines show the inversion response of the original inversion model; the dashed lines show the computed response of the model with the added gravity anomaly. **(c)** The map shows station locations colored by r.m.s. misfit ratio (station misfit with G1 added divided by original station misfit). Higher ratios indicate greater increases in misfit. No site had r.m.s. misfit ratio less than 0.90 so any decrease in r.m.s. is negligible. The small star denotes site LDM013 which had the highest r.m.s. misfit ratio (2.29) with an increase from 0.82 to 1.88. The approximate location of G1 is shown with a black rectangle. BC = Baños Campanario; CC = Cerro Campanario. (For interpretation of the references to color in this figure, the reader is referred to the web version of this article.)

melt fractions greater than 35% to explain the modeled bulk resistivity under the assumption that the petrological estimates are valid for C4 (Fig. 5(b) and 5(c)).

5.2.2. South of LdM

There are no major conductive features imaged to the south of LdM and much of the southeast LdM basin is resistive at depth (R1; see Figs. 3 and 4). This is surprising given the large volume of post-glacial erupted material to the southeast of LdM.

The lack of conductors to the south and east makes it unlikely that the entire LdMVF is underlain by a large crystal-poor reservoir. To test this hypothesis, a continuous, 0.5 Ωm conductive layer was added to the original inversion model at a depth of 4 km and with a spatial extent matching the extent of LdMVF (Fig. 9a). The layer (M1) has a thickness of 500 m and represents a continuous, crystal-poor (85%) rhyolite reservoir at a temperature of 800 °C and 5 wt% H_2O (Fig. 6). The shape of the added anomaly was chosen to encompass most of the vents around LdMVF. Large changes to r.m.s. misfit are seen at sites around much of LdM with maximum discrepancies at sites in the southeast (Fig. 9b). At site LDM008, the r.m.s. misfit increased from 0.73 in the original inversion, to 3.29 in the edited model and large discrepancies were seen in all impedance components. Total r.m.s. misfit increased to 2.24 for all data points and most of this increase occurred at frequencies less than 1 Hz.

A shallow (<5 km), crystal-rich, rhyolite mush underlying the entire LdMVF is consistent with the MT data provided that the melt is relatively anhydrous, has relatively low melt fraction, and is at the lower end of temperature estimates from petrological data. For example, a 25% melt fraction mush with 1 wt% H_2O at 760 °C results in a bulk resistivity of approximately 20 Ωm (Fig. 5(a), Fig. 6). Given the overlying conductor (C1) which attenuates signal, it would be unlikely that MT could detect such a mush zone, even if it were 500 m thick (see Supplementary Material 5). The lack of large conductors beneath LdMVF provides an important petrological constraint and this interpretation is consistent with the inferred 115 km^3 mush zone imaged by Bouguer gravity data which Miller et al. (2017a) suggested was anhydrous (1 wt% H_2O) and relatively low melt fraction (30%).

6. Implications for magma dynamics and conclusions

The MT model suggests that the LdMVF is fed from a multi-chamber magmatic column with a large, deep (>8 km), melt

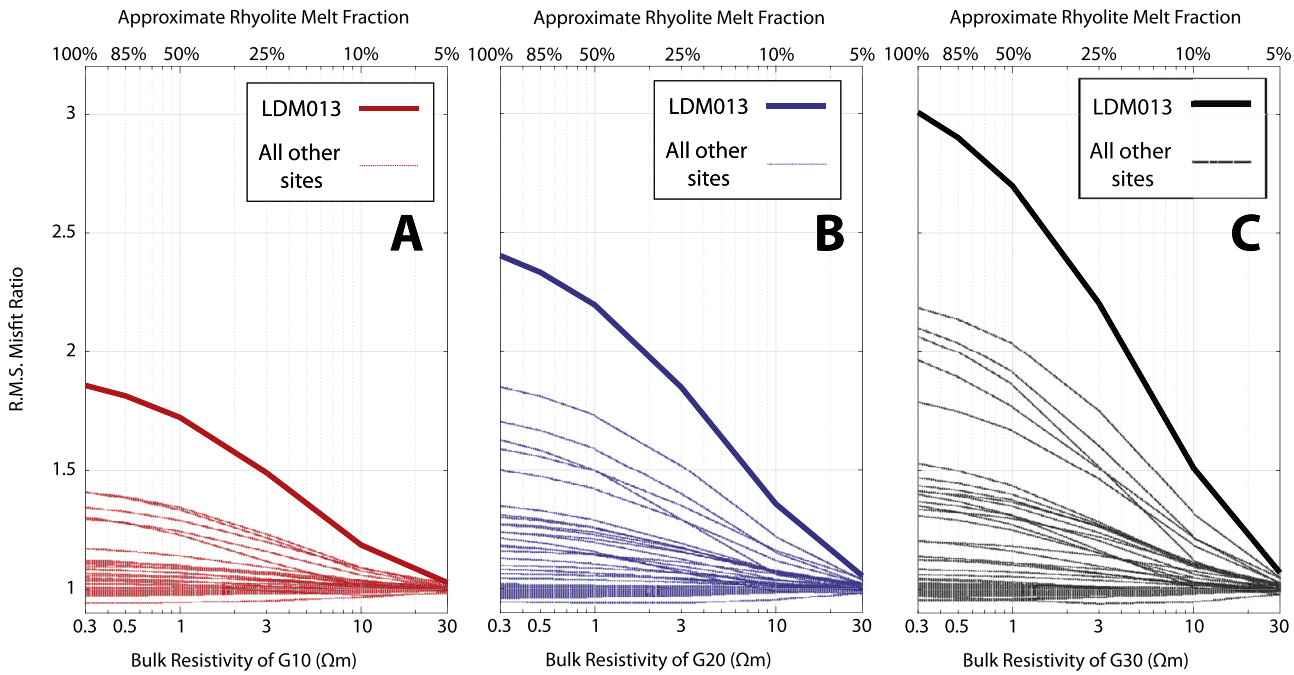

Fig. 8. R.M.S. misfit ratio for each MT site as a function of the bulk resistivity for the anomalies **(a)** G10 (10 km^3), **(b)** G20 (20 km^3), and **(c)** G30 (30 km^3), which were added to the original inversion model. Each plot shows how r.m.s. misfit changed for each station (thin, dashed lines) with site LDM013 highlighted (thick line). Lower bulk resistivities on each plot show larger increases in r.m.s. misfit. Larger anomalies (G30) show larger increases in r.m.s. misfit than small anomalies (G10). Most sites have r.m.s. misfit ratios near 1 because they are far from the anomaly and not influenced by it, regardless of the anomaly's size or bulk resistivity. However, more sites see increases in r.m.s. misfit ratio (>1.5) for the larger anomaly, G30. The MT data at all sites is relatively insensitive to the small anomaly (G10), regardless of the bulk resistivity of the anomaly.

region to the north (C4) providing heat and melt to shallower (<5 km depth), zones beneath the LdMVF. This heat and melt injection allows for the formation of volumes of melt and hydrothermal fluids in the northwest LdMVF (C3). An even shallower anomaly (<3 km depth) identified with Bouguer gravity data is located directly beneath LdM. MT forward modeling tests show that this anomaly (G1) is unlikely to be a large (30 km^3), high melt fraction (>50%) anomaly. However, a smaller (e.g. 10–20 km^3) or lower melt fraction magma body would not be detectable with MT. This shallow feature (G1) may be part of a larger crystal mush zone as suggested by Andersen et al. (2017) which is reactivated by heat and melt from C4. However, such a shallow mush would need to have very low water content (1%) and very low temperature (760 °C) in order to go undetected by MT.

The fact that C4 underlies the inferred outline of the 950 ka Bobadilla caldera from Hildreth et al. (2010) suggests that C4 may be a large, long-lived region of warm storage responsible for the largest observed eruptions in the LdMVF. Mafic recharge from the lower crust is required to maintain a large zone of partial melt at 9 km depth for 1 Ma. However, intrusion rates do not need to be high and could be as low as 10^{-4} km^3/yr assuming the lower crust (>25 km depth) is considered thermally mature (Karakas et al., 2017).

Crucially, the deepest conductive region (C4) lies outside the zone of deformation and beyond the edge of any post-glacial vents or lava flows. No major conductive features are imaged to the south or southeast of the LdM basin and, in fact, much of this region is resistive at depth. This implies that source melts for the northwestern vents in the LdMVF travel both vertically and laterally (5–10 km) as they migrate to the surface. The progression from C4 to C3 to G1 shows a potential pathway from deeper, northern source regions to shallow regions directly beneath the LdMVF (Fig. 4). This interpretation is not conventional in terms of conceptual magma plumbing models which generally assume purely vertical ascent; however such distances are not unreasonable and have been seen at other volcanos and calderas (Hill et al., 2009; Kelbert et al., 2012; Aizawa et al., 2014; Cashman and Giordano, 2014). This has implications for magma transport mechanisms, local structural stress regimes at LdMVF, and the source material for the observed inflation.

The MT model and interpretation presented here suggests that there is a difference between the southeast and northwest LdMVF in terms of melt generation and fluid transport since the northwest contains significant conductive anomalies (C3 and C4) while the southeast is largely resistive (R1). However, the southeast also contains large volumes of post-glacial rhyolite so it is important to ask where the magma and heat that drives these eruptions is coming from. Two possible explanations can be offered. The first is that the large volume of melt to the north (C4) is providing heat and melt to both the northwest and southeast LdMVF. This would require relatively long lateral distances (e.g. >20 km from C4 to Barrancas vents) and there is little geological evidence to support this interpretation. The second possibility is that the erupted lavas in the northwest and southeast have two different source regions with the southeast source region being too deep to be resolved with the current MT array or beyond the edges of the current MT array. Petrological evidence from Andersen et al. (2017) showed that there is a compositional distinction between the post-glacial lavas in the northwest and southeast LdMVF. There is further evidence that the Troncoso fault may be an important structural lineament separating a fractured and faulted zone to the northwest from a relatively un-faulted zone to the southeast (Keranen et al., 2016). The MT model and interpretation, along with these other lines of evidence, support the possibility that the source regions of melt for the southeast and northwest vents are different. More geophysical and geological evidence is necessary to better understand the source regions for the southeast vents of the LdMVF including further exploration in Argentina and more detailed study of the Barrancas complex.

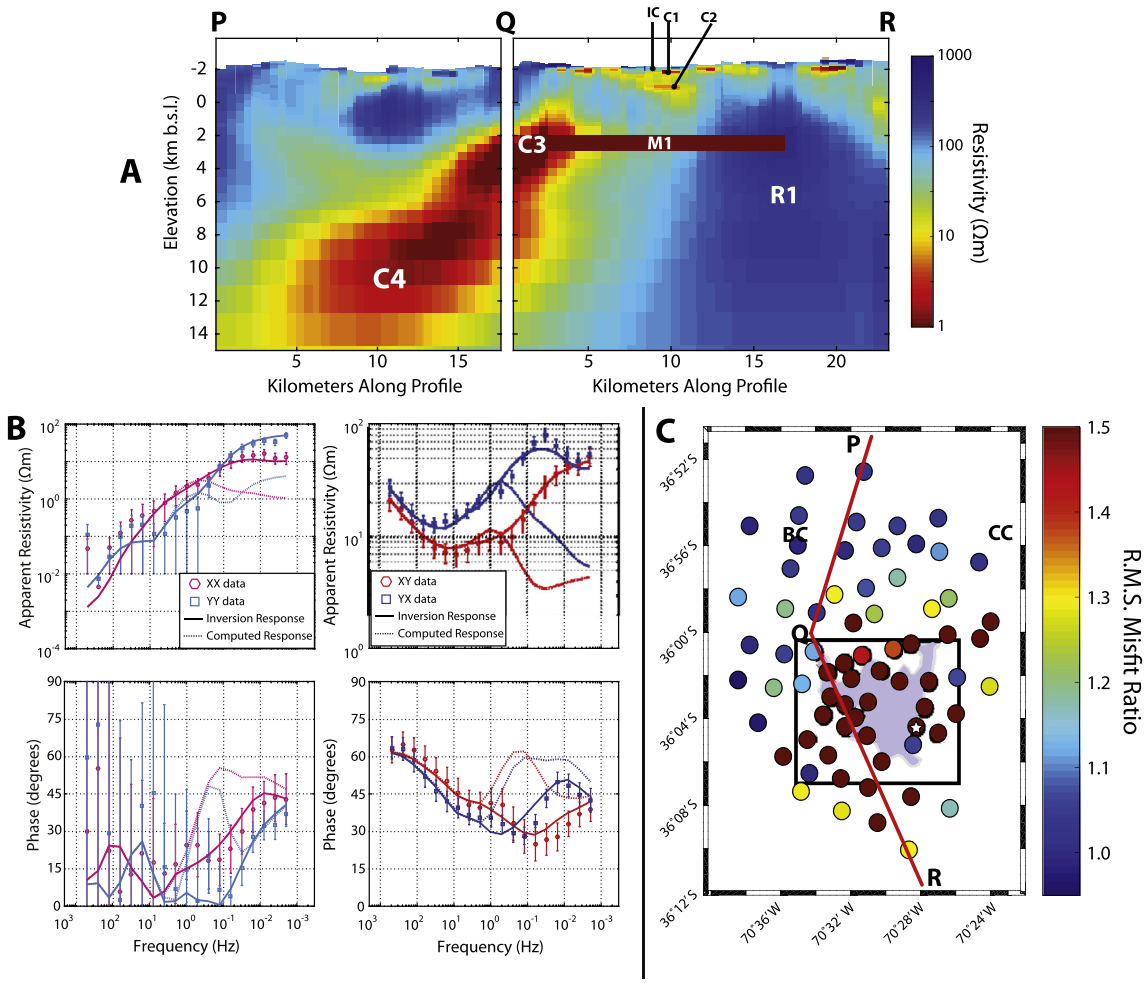

Fig. 9. Sensitivity analysis for a uniform, 0.5 Ωm, 500 m thick layer underlying a large portion of the Laguna del Maule Volcanic Field. The anomaly represents a large, crystal-poor magma reservoir with 85% rhyolitic melt. **(a)** The top panel shows the same diagonal fence diagram from Fig. 4 along PQR through the inversion model with the M1 anomaly added. **(b)** The apparent resistivity and phase of the impedance tensor components as a function of frequency for site LDM008. The red and pink hexagons with errors bars show the xy and xx data, respectively, as a function of frequency. The blue and light blue circles with error bars show the yx and yy data, respectively. The solid lines show the inversion response of the original inversion model; the dashed lines show the computed response of the model with the added layer. **(c)** The map shows station locations colored by r.m.s. misfit ratio (station misfit with M1 added divided by original station misfit). Higher ratios indicate greater increases in misfit. No site had r.m.s. misfit ratio less than 0.90 so any decrease in r.m.s. is negligible. The small star denotes site LDM008 which had the highest r.m.s. misfit ratio (4.51) with an increase from 0.73 to 3.29. The approximate location of M1 is shown with a black rectangle. BC = Baños Campanario; CC = Cerro Campanario. (For interpretation of the references to color in this figure, the reader is referred to the web version of this article.)

Acknowledgements

This research has been supported by the National Science Foundation (grant number EAR-1411779) and the National Sciences and Engineering Research Council of Canada (NSERC) through a Discovery Grant to MJU and a PGS-D scholarship to DC. We thank Gary Egbert and Anna Kelbert for the use of their ModEM inversion program and special thanks to Naser Meqbel for providing assistance and support. WestGrid computer clusters were used for 3-D inversion and forward modeling. We thank Cathy Hickson, Carolina Rodriguez and Alterra Power Corp (now Energy Development Corporation) for providing 2009 to 2010 MT data. Thank you to Wolfgang Soyer and CGG for processing the MT data. Special thanks to the Centro de Excelencia en Geotermia de Los Andes (FONDAP 15090013) and Universidad Católica de Chile for use of Metronix MT instruments. Many individuals were involved with field work and other logistical support including Bárbara Blanco, Daniel Cabrera, Matthew Comeau, Ariel Figueroa, Jorge Gacitua, Maria Jose Hernández, Maximiliano Pavez, Valentina Reyes-Wagner, Brad Singer, and Cliff Thurber. Thank you to Omar Reyes, Luis Burgos, and Familia Rancho Los Reyes for the horse adventures. Special thanks to Don Luis Torres for his invaluable knowledge of Laguna del Maule and his logistical support. Thank you to many members of the LdM research team for important discussions regarding the interpretation, especially Nathan Andersen, Ninfa Bennington, Hélène Le Mével, and Craig Miller. We gratefully thank the additional input from two anonymous reviewers who helped improve the manuscript.

Appendix A. Supplementary material

Supplementary material related to this article can be found online at https://doi.org/10.1016/j.epsl.2018.01.007.

References

Aizawa, K., et al., 2014. Three-dimensional resistivity structure and magma plumbing system of the Kirishima Volcanoes as inferred from broadband magnetotelluric data. J. Geophys. Res., Solid Earth 119, 198–215. https://doi.org/10.1002/2013JB010682.Received.

Andersen, N.L., Singer, B.S., Jicha, B.R., Beard, B.L., Johnson, C.M., Licciardi, J.M., 2017. Pleistocene to Holocene growth of a large upper crustal rhyolitic magma reservoir beneath the active Laguna del Maule Volcanic Field, central Chile. J. Petrol. 58 (1), 85–114. https://doi.org/10.1093/petrology/egx006.

Bachmann, O., Bergantz, G., 2008. The magma reservoirs that feed supereruptions. Elements 4 (1), 17–21. https://doi.org/10.2113/GSELEMENTS.4.1.17.
Beamish, D., Travassos, J.M., 1992. The use of the D+ solution in magnetotelluric interpretation. J. Appl. Geophys. 29 (1), 1–19.
Benavente, O., Tassi, F., Reich, M., Aguilera, F., Capecchiacci, F., Gutiérrez, F., Vaselli, O., Rizzo, A., 2016. Chemical and isotopic features of cold and thermal fluids discharged in the Southern Volcanic Zone between 32.5°S and 36°S: insights into the physical and chemical processes controlling fluid geochemistry in geothermal systems of Central Chile. Chem. Geol. 420, 97–113. https://doi.org/10.1016/j.chemgeo.2015.11.010.
Booker, J.R., 2014. The magnetotelluric phase tensor: a critical review. Surv. Geophys. 35 (1), 7–40. https://doi.org/10.1007/s10712-013-9234-2.
Caldwell, T.G., Bibby, H.M., Brown, C., 2004. The magnetotelluric phase tensor. Geophys. J. Int. 158 (2), 457–469. https://doi.org/10.1111/j.1365-246X.2004.02281.x.
Cardona, C.E., Tassara, A., Cruz, G., Lara, L.E., Morales, S., Kohler, P., Franco, L., 2018. Crustal seismicity associated to rapid surface uplift at Laguna del Maule Volcanic Complex, Southern Volcanic Zone of the Andes. J. Volcanol. Geotherm. Res., https://doi.org/10.1016/j.jvolgeores.2018.01.009.
Cashman, K.V., Giordano, G., 2014. Calderas and magma reservoirs. J. Volcanol. Geotherm. Res. 288, 28–45. https://doi.org/10.1016/j.jvolgeores.2014.09.007.
Chaussard, E., Amelung, F., 2014. Regional controls on magma ascent and storage in volcanic arcs. Geochem. Geophys. Geosyst. 15, 1407–1418. https://doi.org/10.1002/2015GC005918.Received.
Chave, A.D., Jones, A.G., 2012. The Magnetotelluric Method – Theory and Practice. Cambridge University Press, Cambridge, UK.
Comeau, M.J., Unsworth, M.J., Cordell, D., 2016. New constraints on the magma distribution and composition beneath Volcán Uturuncu and the southern Bolivian Altiplano from magnetotelluric data. Geosphere 12 (5), 1391–1421. https://doi.org/10.1130/GES01277.1.
Feigl, K.L., Le Mevel, H., Tabrez Ali, S., Cordova, L., Andersen, N.L., DeMets, C., Singer, B.S., 2013. Rapid uplift in Laguna del Maule volcanic field of the Andean Southern Volcanic zone (Chile) 2007–2012. Geophys. J. Int. 196 (2), 885–901. https://doi.org/10.1093/gji/ggt438.
Glover, P.W.J., Hole, M.J., Pous, J., 2000. A modified Archie's law for two conducting phases. Earth Planet. Sci. Lett. 180 (3–4), 369–383. https://doi.org/10.1016/S0012-821X(00)00168-0.
Guo, X., Zhang, L., Behrens, H., Ni, H., 2016. Probing the status of felsic magma reservoirs: constraints from the P–T–H_2O dependences of electrical conductivity of rhyolitic melt. Earth Planet. Sci. Lett. 433, 54–62. https://doi.org/10.1016/j.epsl.2015.10.036.
Guo, X., Li, B., Ni, H., Mao, Z., 2017. Electrical conductivity of hydrous andesitic melts pertinent to subduction zones. J. Geophys. Res., Solid Earth 122 (3), 1777–1788. https://doi.org/10.1002/2016JB013524.
Heise, W., Caldwell, T.G., Bibby, H.M., Bennie, S.L., 2010. Three-dimensional electrical resistivity image of magma beneath an active continental rift, Taupo Volcanic Zone, New Zealand. Geophys. Res. Lett. 37 (10), 2–6. https://doi.org/10.1029/2010GL043110.
Hickson, C.J., et al., 2011. The Mariposa Geothermal System, Chile. GRC Trans. 35, 817–826.
Hildreth, W., Singer, B., Godoy, E., Munizaga, F., 1998. The age and constitution of cerro campanario, a mafic stratovolcano in the Andes of Central Chile. Rev. Geol. Chile 25 (1), 17–28. https://doi.org/10.4067/S0716-02081998000100002.
Hildreth, W., Godoy, E., Fierstein, J., Singer, B., 2010. Laguna del Maule volcanic field: eruptive history of a Quaternary basalt-to-rhyolite distributed volcanic field on the Andean range crest in central Chile. Serv. Nac. Geol. y Minería, Boletin 63.
Hill, G.J., Caldwell, T.G., Heise, W., Chertkoff, D.G., Bibby, H.M., Burgess, M.K., Cull, J.P., Cas, R.A.F., 2009. Distribution of melt beneath Mount St Helens and Mount Adams inferred from magnetotelluric data. Nat. Geosci. 2 (11), 785–789. https://doi.org/10.1038/ngeo661.
Jones, A.G., 1999. Imaging the continental upper mantle using electromagnetic methods. Lithos 48, 57–80.
Karakas, O., Degruyter, W., Bachmann, O., Dufek, J., 2017. Lifetime and size of shallow magma bodies controlled by crustal-scale magmatism. Nat. Geosci. 10, 446–450. https://doi.org/10.1038/NGEO2959.
Kelbert, A., Egbert, G.D., DeGroot-Hedlin, C., 2012. Crust and upper mantle electrical conductivity beneath the Yellowstone Hotspot Track. Geology 40 (5), 447–450. https://doi.org/v10.1130/G32655.1.
Kelbert, A., Meqbel, N., Egbert, G., Tandon, K., 2014. ModEM: a modular system for inversion of electromagnetic geophysical data. Comput. Geosci. 66, 40–53. https://doi.org/10.1016/j.cageo.2014.01.010.
Keranen, K., Peterson, D.E., Miller, C.A., Garibaldi, N., Tikoff, B., Williams-Jones, G., 2016. Magma–tectonic interaction at Laguna del Maule, Chile. In: AGU Fall Meeting V53C-3121. San Francisco, CA.
Larsen, J.C., Mackie, R.L., Manzella, A., Fiordelisi, A., Rieven, S., 1996. Robust smooth magnetotelluric transfer functions. Geophys. J. Int. 124 (3), 801–819. https://doi.org/10.1111/j.1365-246X.1996.tb05639.x.
Laumonier, M., Gaillard, F., Sifre, D., 2015. The effect of pressure and water concentration on the electrical conductivity of dacitic melts: implication for magnetotelluric imaging in subduction areas. Chem. Geol. 418, 66–76. https://doi.org/10.1016/j.chemgeo.2014.09.019.
Laumonier, M., Gaillard, F., Muir, D., Blundy, J., Unsworth, M., 2017. Giant magmatic water reservoirs at mid-crustal depth inferred from electrical conductivity and the growth of the continental crust. Earth Planet. Sci. Lett. 457, 173–180. https://doi.org/10.1016/j.epsl.2016.10.023.
Le Mével, H., Gregg, P.M., Feigl, K.L., 2016. Magma injection into a long-lived reservoir to explain geodetically measured uplift: application to the 2007–2014 unrest episode at Laguna del Maule volcanic field, Chile. J. Geophys. Res., Solid Earth 121 (8), 6092–6108. https://doi.org/10.1002/2016JB013066.
Miller, C.A., Williams-Jones, G., Fournier, D., Witter, J., 2017a. 3D gravity inversion and thermodynamic modelling reveal properties of shallow silicic magma reservoir beneath Laguna del Maule, Chile. Earth Planet. Sci. Lett. 459, 14–27. https://doi.org/10.1016/j.epsl.2016.11.007.
Miller, C.A., Le, Mével H., Currenti, G., Williams-Jones, G., Tikoff, B., 2017b. Microgravity changes at the Laguna del Maule volcanic field: magma-induced stress changes facilitate mass addition. J. Geophys. Res., Solid Earth, 1–18. https://doi.org/10.1002/2017JB014048.
Muñoz, G., 2014. Exploring for geothermal resources with electromagnetic methods. Surv. Geophys. 35 (1), 101–122. https://doi.org/10.1007/s10712-013-9236-0.
Newman, G., Wannamaker, P., Hohmann, G., 1985. On the detectability of crustal magma chambers using the magnetotelluric method. Geophysics 50 (7), 1136–1143.
Ni, H., Keppler, H., Behrens, H., 2011. Electrical conductivity of hydrous basaltic melts: implications for partial melting in the upper mantle. Contrib. Mineral. Petrol., 637–650. https://doi.org/10.1007/s00410-011-0617-4.
Ogawa, Y., Ichiki, M., Kanda, W., Mishina, M., Asamori, K., 2014. Three-dimensional magnetotelluric imaging of crustal fluids and seismicity around Naruko volcano, NE Japan. Earth Planets Space 66 (158), 1–13.
Parker, R., Whaler, K., 1981. Numerical methods for establishing solutions to the inverse problem of electromagnetic induction. J. Geophys. Res., Solid Earth 86, 9574–9584.
Parker, R.L., 2010. Can a 2-D MT frequency response always be interpreted as a 1-D response? Geophys. J. Int. 181 (1), 269–274. https://doi.org/10.1111/j.1365-246X.2010.04512.x.
Pritchard, M.E., Gregg, P.M., 2016. Geophysical evidence for silicic crustal melt in the continents: where, what kind, and how much? Elements 12 (2), 121–127. https://doi.org/10.2113/gselements.12.2.121.
Ramos, V.A., Litvak, V.D., Folguera, A., Spagnuolo, M., 2014. An Andean tectonic cycle: from crustal thickening to extension in a thin crust (34°–37° SL). Geosci. Front. 5 (3), 351–367. https://doi.org/10.1016/j.gsf.2013.12.009.
Ranganayaki, R.P., 1984. An interpretive analysis of magnetotelluric data. Geophysics 49 (10), 1730–1748.
Reyes-Wagner, V., Díaz, D., Cordell, D., Unsworth, M., 2017. Regional electrical structure of the Andean subduction zone in central Chile (35°–36°S) using magnetotellurics. Earth Planets Space 69, 1–9. https://doi.org/10.1186/s40623-017-0726-z.
Rosenberg, C., Handy, M., 2005. Experimental deformation of partially melted granite revisited: implications for the continental crust. J. Metamorph. Geol. 24, 19–28. https://doi.org/10.1111/j.1525-1314.2005.00555.x.
Self, S., 2006. The effects and consequences of very large explosive volcanic eruptions. Philos. Trans. R. Soc. A Math. Phys. Eng. Sci. 364 (1845), 2073–2097. https://doi.org/10.1098/rsta.2006.1814.
Singer, B., et al., 2014. Dynamics of a large, restless, rhyolitic magma system at Laguna del Maule, southern Andes, Chile. GSA Today 12, 4–11. https://doi.org/10.1130/GSATG216A.1.
Unsworth, M., Rondenay, S., 2013. Mapping the distribution of fluids in the crust and lithospheric mantle utilizing geophysical methods. In: Harlov, D.E., Austrheim, H. (Eds.), Metasomatism and the Chemical Transformation of Rock. Springer Berlin Heidelberg, Berlin, Germany, pp. 535–598.
USGS, 2017. National Water Information System: web interface. Available from https://waterdata.usgs.gov/nwis/ (Accessed 23 June 2017).
Wannamaker, P.E., Evans, R.L., Bedrosian, P.A., Unsworth, M.J., Maris, V., McGary, R.S., 2014. Segmentation of plate coupling, fate of subduction fluids, and modes of arc magmatism in Cascadia, inferred from magnetotelluric resistivity. Geochem. Geophys. Geosyst. 15 (11), 4230–4253. https://doi.org/10.1002/2014GC005509.